

M&MoCS



Shahid Chamran
University of Ahvaz

Journal of Applied and Computational Mechanics



Research Paper

Nonlinear Buckling and Post-buckling of Shape Memory Alloy Shallow Arches

George C. Tsiatas¹, Ioannis N. Tsiptsis², Antonis G. Siokas³

¹ Department of Mathematics, University of Patras

University Campus, Rio, GR-26504, Greece, Email: gtsiatas@upatras.gr

² Department of Civil, Geo and Environmental Engineering, Technische Universität München

Arcisstr. 21, Munich, D-80333, Germany, Email: ioannis.tsiptsis@tum.de

³ School of Civil Engineering, National Technical University of Athens

Zografou Campus, Athens, GR-15773, Greece, Email: antonissiokas@gmail.com

Received November 29 2019; Revised December 03 2019; Accepted for publication December 04 2019.

Corresponding author: G.C. Tsiatas (gtsiatas@upatras.gr)

© 2020 Published by Shahid Chamran University of Ahvaz

& International Research Center for Mathematics & Mechanics of Complex Systems (M&MoCS)

Abstract. In this work, the nonlinear buckling and post-buckling behavior of shallow arches made of Shape Memory Alloy (SMA) is investigated. Arches are susceptible to large deflections, due to their slenderness, especially when the external load exceeds the serviceability limit point. Beyond this, loss of stability may occur, the famous snap-through buckling. For this reason, curved beams can be used in passive vibration control devices for seismic response mitigation, and the geometrically nonlinear analysis is needed for the accurate prediction of their response. Thus, in this research effort, the assumptions of the Euler-Bernoulli beam theory are considered, and the Von Karman strain field is employed to account for large deflections. The formulation of the problem is displacement-based regarding the axial (tangential) and transverse (normal) displacements, while the two governing equations are coupled and nonlinear. In order to introduce the SMA constitutive law, the stress-strain experimental curves described in the literature are employed together with a fiber approach at specific control cross-sections along the beam. The numerical solution of the longitudinal problem is achieved using the Analog Equation Method (AEM), a Boundary Element Method (BEM) based technique, and the iterative procedure is based on a Newton-Raphson scheme by using a displacement control algorithm to trace the fully nonlinear equilibrium path and overcome the limit points. Several representative examples are studied, not only to validate the proposed model but also to investigate the nonlinear buckling and post-buckling of SMA shallow arches.

Keywords: Shallow arches, Shape Memory Alloys, Buckling, Nonlinear Analysis, Fiber Approach.

1. Introduction

During the last decades, there is an increasing interest in the development and integration of smart materials into structures due to their outstanding behavior under severe loading conditions (e.g., earthquakes). These kinds of materials can usually adjust their properties to provide various functions that improve the overall behavior of structures and mitigate their damage. Shape memory alloys (SMAs), as a class of intelligent materials, exhibit an exemplary performance and have been applied in many structural sectors, such as aerospace, robotics, biomedical, civil [1] due to their ability to recover their shape by heating or mechanical unloading after sustaining severe deformation. This kind of material exhibits an ordered crystal structure meaning that atoms have specific locations in a lattice-like formulation. SMAs have two unique

properties, namely, shape memory effect (SME) or thermoelasticity and superelasticity or pseudoelasticity (PE) due to the nonlinear stress-strain curve that describes the SMAs' behavior. The SME refers to the phenomenon that SMAs return to their original shapes upon heating. The superelasticity, realized later than the SME, refers to the phenomenon that SMAs can undergo a large amount of inelastic deformations (up to 15%) and recover their shapes after unloading at a constant temperature. The loading paths are not identical to the unloading ones, and as a result stress-strain hysteresis loops are formed. These unique properties are the result of reversible phase transformations between more-ordered (austenitic) and less-ordered product (martensitic) crystallographic structures under stress and/or temperature variations [2-5]. The transformations are diffusionless and take place through atomic movements, which are less than one atomic spacing. The SMA which is most commonly used in applications is Nitinol (NiTi), composed of nickel and titanium, which possesses superior thermomechanical and thermoelectrical properties [6]. In most NiTi-SMA devices, the structural elements that have been employed are beams, bars or cables (e.g. in passive, active and semi-active control of civil structures [1]), and, thus, can be simulated by one-dimensional models. SMA beams have been utilized as actuators, energy harvesters, and health monitoring devices for structures. The resisting mechanism of SMA beams in most applications is through bending.

Together with the beam theory employed to simulate the SMA structures, an appropriate constitutive model is highly crucial since the conventional theories or laws cannot describe the response of SMA structural elements. During the first studies, the proposed models were either not able to predict the SME [7-8] behavior or their focus was only on the PE keeping the temperature constant in order to simplify the problem under investigation (e.g., uniaxial tension stress-strain response [9], pure bending of an Euler-Bernoulli beam [10]). Both one [9-10] and three-dimensional [11] constitutive models have been developed reproducing the PE and following simplifying assumptions (isotropy). The formulations developed in the studies mentioned above [9-10] allow for different elastic properties between austenite and martensite. Additionally, the formulation in [10] accounts for tensile-compressive asymmetry, which is discussed below, since the bending problem is examined. Various homogenization schemes reported in the literature, such as Mori-Tanaka [12], Reuss [9], Voigt [9], have been employed for the derivation of the elastic modulus tensor and the results have been validated against experiments [9]. More elaborate SMA constitutive models have also been developed to predict both PE and SME for both one- or three-dimensional models [13-15] allowing for more accurate computer-aided analysis of SMA structures under various loading. The 1-D constitutive model reported in [13], which is the first model able to predict the SME, has been employed in the analysis of composite beams with SMA inclusions [16-17]. Moreover, the 3-D constitutive SMA model reported in [14] and its improved form [15] have also been employed in recent studies on SMA beams [18-19]. Except for the primary phases mentioned above (SME and PE), secondary phases might also need to be considered. These are related to incomplete phase transformation and asymmetric behavior in tension and compression [10, 20]. Several research efforts proposed relevant one-, two- or three-dimensional models that consider the differences between the elastic properties and responses of SMAs [21-25]. The models above are generally employed up to now in order to study the behavior of beams under bending and are usually integrated with the Finite Element Method (FEM). In an effort to reduce the computational cost of the existing numerical SMA models, analytical solutions have also been proposed describing both SME and PE as well as addressing limitations related to asymmetric compression-tensile stresses [26] or different stiffness of austenite and martensite [27-29]. To gain a more comprehensive understanding of the mechanical responses of superelastic SMAs, several experiments have been performed on NiTi cylindrical SMA bars under uniaxial tension, compression, bending, and/or buckling [30-31]. Additionally, SMA material stress-strain experimental curves fitted by polynomials have also been adopted in order to develop simplified computational tools for the investigation of SMA beams sustaining large deformations [32].

Since the classical beam theory assumption that plane cross-sections remain both plane and perpendicular to the longitudinal axis of the SMA beam is proved experimentally to be not valid [31], the use of more elaborate beam models becomes essential. Towards more accurate solutions and based on a simple 1D superelastic constitutive law, analytical moment-curvature relations for SMA beams have been reported in the literature throughout the years [2, 26, 33-34]. However, to reduce the complexity of the analytical formulation, many studies employ classical Euler-Bernoulli theory (EBT) to study the deformations of SMA beams under various loading [10, 18, 20, 26, 35, 36]. In [20], the bending of a composite beam is studied through a semi-analytical method instead of the commonly used FEM. Contrary to many other studies that employ EBT, the location of the cross section's neutral axis is considered as an unknown in [20]. Moreover, the bending-curvature analytical expression is obtained in [26] employing the assumptions of EBT. Based on the EBT, the dynamic behavior of SMA beams considering PE effect has also been studied for forced or free vibrations [19]. In other studies, the Kirchhoff hypothesis is employed together with the EBT's assumptions in order to account for geometric nonlinearities of SMA beams under combined tension and bending [32]. Finally, thermo-mechanical studies of SMA structures have been performed with the aid of EBT [35-36]. Towards more accurate modeling of SMA beams in bending with loading and unloading cycles, the Timoshenko beam theory (TBT) has been employed in order to derive moment-curvature and shear force-strain relations or generally study the bending behavior of superelastic SMA beams [2, 29, 37-38]. Additionally, employing a nonlinear large deformation theory (von Kármán strain field) and Brinson SMA the EBT's assumptions, the behavior of beams with SMAs under tension-compression tests at different temperatures as well as under loading-heating (or heating-loading) paths have been examined [39]. Other very recent studies employ the von Kármán strain-displacement relation and the one-dimensional model [13] to study analytically the thermal buckling, and post-buckling behavior of composite beam reinforced with SMAs [40]. In a similar concept, the Brinson model is employed together with the von Kármán strain-displacement fields and the TBT in order to investigate the nonlinear thermal buckling of functionally graded beams with SMA layers [41]. Yet the investigation of buckling and post-buckling behavior is still an

open issue for the design of various structural members either initially flat, such as beams [42, 43] and plates [44-46], or initially curved, for example, shells [47-51]. Recently, Tsiatas et al. [52] introduced a new layered approach to the nonlinear analysis of initially straight Euler-Bernoulli beams by the Boundary Element Method (BEM). The beam was made of a superelastic Shape Memory Alloy (SMA) and studied in the context of both geometrical and material nonlinearity. To the authors' knowledge, there is not reported formulation of SMA models that consider a shallow arch geometry directly in the derivation of equilibrium equations and the nonlinear regime.

In this work, the nonlinear buckling and post-buckling behavior of shallow arches made of SMAs is investigated. Curved beams are often used in several engineering fields such as civil, mechanical, and aeronautical engineering. It is well known that arches are susceptible to large deflections, due to their slenderness, especially when the external load exceeds the serviceability limit point. Beyond this, loss of stability may occur, the famous snap-through buckling [53]. Such systems are known as bi-stable systems; that is, they present two distinct stable configurations under identical loading conditions. During the transition between these configurations, the system exhibits negative stiffness characteristics while mechanical energy is dissipated. For this reason, arches can be used in passive vibration control devices for seismic response mitigation [54, 55], and the geometrically nonlinear analysis is needed for the accurate prediction of their response. Thus, in this research effort, the assumptions of the Euler-Bernoulli beam theory are considered, and the Von Karman strain field is employed to account for large deflections. Notably, the beam undergoes large displacements with small strain and moderate rotations (intermediate nonlinear theory) under general boundary conditions which may be nonlinear. The formulation of the problem is displacement-based regarding the axial (tangential) and transverse (normal) displacements, while the two governing equations are coupled and nonlinear. In order to introduce the SMA constitutive law, the stress-strain experimental curves described in [32] and [52] are employed together with a fiber approach at specific control cross-sections along the beam. However, a similar method can be followed in order to develop beam models made of other SMA (e.g., iron-based SMAs) if an appropriate constitutive model is utilized. The numerical solution of the longitudinal problem is achieved using the Analog Equation Method (AEM), a Boundary Element Method (BEM) based technique [56]. The iterative procedure is based on a Newton-Raphson scheme by using a displacement control algorithm to trace the fully nonlinear equilibrium path and overcome the limit points. The novelty of this work lies in the investigation of the nonlinear buckling and post-buckling of SMA shallow arches through a reliable and robust numerical method which can handle any given nonlinear constitutive law.

2. Statement of the Problem

Let us consider a curved beam with a centroidal axis that lies in the xz plane. The initial radius of curvature is denoted by R . A curvilinear coordinate system (s, n, t) is employed. The s coordinate spans the centroidal axis of the undeformed curved beam, while n is the radial coordinate and t is normal to the plane of the paper (see Fig. 1a). The beam has a uniform cross-section, i.e. the axial EA and bending stiffness EI are constant, and it is subjected to the distributed load $p_n = p_n(s)$ along the radial direction (see Fig. 1b).

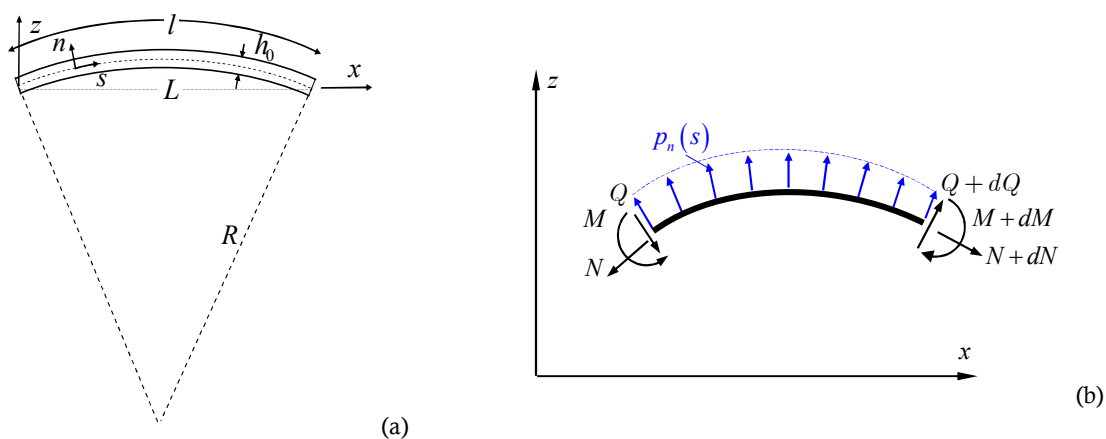


Fig. 1. (a) Geometry of the shallow arch and (b) conventional positive forces and moments acting on an infinitesimal curved element.

Considering the cross-sectional deformations, the Euler-Bernoulli assumptions hold. The nonlinear strain-displacement relations are obtained following the general shell theory simplified for cylindrical shells [57]. More specifically, the von Kármán axial nonlinear strain for straight beams is augmented with the term w/R which represents the increase in length due to the displacement w [58]. The analysis is performed in the context of small strains-moderately large rotations which allows us to retain the nonlinear term $w_{,s}^2$ and to omit the nonlinear terms $(u/R)^2$ and $uw_{,s}/R$ of the non-linear strain-displacement relation [59]. Note that, $u = u(s)$ is the axial and

$w = w(s)$ the normal displacement (opposite to the radial direction as in Fig. 1a) of the centroid, respectively, and $(\bullet)_{,s}$, $(\bullet)_{,ss}$ denote the first and second derivative with respect to s .

The simplified Green-Lagrange strain $\epsilon = \epsilon(s, z)$ (with $\epsilon_{zz} = 0$) [60] at an arbitrary point (s, z) on the cross-section of a curved beam can be decomposed into a membrane ϵ_m and a bending ϵ_b component [52]

$$\epsilon(s, z) = \epsilon_m + \epsilon_b, \tag{1}$$

which can be written as

$$\epsilon_m = u_{,s} + \frac{w}{R} + \frac{1}{2}w_{,s}^2, \quad \epsilon_b = -zw_{,ss}, \tag{2}, (3)$$

Applying the equations of equilibrium at a typical element of length ds with all the pertinent forces acting on it (Fig.1b), the following equations are obtained [53]

$$N_{,s} + \frac{Q}{R} = 0, \tag{4}$$

$$Q_{,s} - \frac{N}{R} + \mathbb{N}(u, w) = -p_n, \tag{5}$$

$$M_{,s} - Q = 0, \tag{6}$$

where

$$\mathbb{N}(u, w) = (Nw_{,s})_{,s}, \tag{7}$$

is the nonlinear term due to the nonlinear strains. Furthermore, the stress resultants appearing in the equilibrium equations, i.e., the axial force, bending moment and shear force are given by the relations

$$N = EA\epsilon_0 = EA\left(u_{,s} + \frac{w}{R} + \frac{1}{2}w_{,s}^2\right), \tag{8}$$

$$M = EI\kappa = -EIw_{,ss}, \tag{9}$$

$$Q = (EI\kappa)_{,s} = -EIw_{,sss}, \tag{10}$$

respectively. Eliminating Q from Eqs. (4) to (6) and substituting the nonlinear term from Eq. (7), the governing equations of the curved beam can be written as

$$N_{,s} + \frac{M_{,s}}{R} = 0, \tag{11}$$

$$M_{,ss} - \frac{N}{R} + (Nw_{,s})_{,s} = -p_n. \tag{12}$$

Equations (11), (12) can as well be written in terms of the displacements, substituting Eqs. (8) and (9) into Eqs. (11) and (12)

$$EA\left(u_{,s} + \frac{w}{R} + \frac{1}{2}w_{,s}^2\right)_{,s} - \frac{EIw_{,sss}}{R} = 0, \tag{13}$$

$$-(EIw_{,ss})_{,ss} - \frac{EA}{R}\left(u_{,s} + \frac{w}{R} + \frac{1}{2}w_{,s}^2\right) + EA\left[\left(u_{,s} + \frac{w}{R} + \frac{1}{2}w_{,s}^2\right)w_{,s}\right]_{,s} = -p_n. \tag{14}$$

The above differential equations are subjected to the corresponding boundary conditions, which are given as

$$a_1u(0) + a_2N(0) = a_3, \quad \bar{a}_1u(l) + \bar{a}_2N(l) = \bar{a}_3, \tag{15}, (16)$$

$$\beta_1w(0) + \beta_2Q(0) = \beta_3, \quad \bar{\beta}_1w(l) + \bar{\beta}_2Q(l) = \bar{\beta}_3, \tag{17}, (18)$$

$$\gamma_1w_{,s}(0) + \gamma_2M(0) = \gamma_3, \quad \bar{\gamma}_1w_{,s}(l) + \bar{\gamma}_2M(l) = \bar{\gamma}_3, \tag{19}, (20)$$



where $a_k, \bar{a}_k, \beta_k, \bar{\beta}_k, \gamma_k, \bar{\gamma}_k$ ($k = 1, 2, 3$) are given constants specified at the boundaries of the beam $x = 0, L$. It should be noted that the boundary conditions in Eqs. (15) through (20) are the most general boundary conditions and may also include elastic support. It is obvious that all types of the conventional boundary conditions (clamped, simply supported, guided edge, etc.) can be derived from these equations by appropriately specifying these functions (e.g. for a clamped beam the only non-zero constants are $a_1 = \bar{a}_1 = \beta_1 = \bar{\beta}_1 = \gamma_1 = \bar{\gamma}_1 = 1$).

3. Numerical Formulation

3.1 The AEM Solution

Following the previous analysis, the geometrically nonlinear problem of Euler-Bernoulli shallow arches reduces in establishing the displacement components $u = u(s)$ and $w = w(s)$ having continuous derivatives up to the second and fourth-order with respect to s , respectively. These two displacement components must satisfy the coupled differential Eqs. (13)-(14) inside the beam, and the boundary conditions are given by Eqs. (15)-(20) at the beam ends. The boundary value problem described by Eqs. (13)-(20) is solved employing the Analog Equation Method. According to the analog equation principle, the two coupled differential Eqs. (13)-(14) are substituted by the following analog equations

Following the previous analysis, the geometrically nonlinear problem of Euler-Bernoulli shallow arches reduces in establishing the displacement components $u = u(s)$ and $w = w(s)$ having continuous derivatives up to the second and fourth-order with respect to s , respectively. These two displacement components must satisfy the coupled differential Eqs. (13)-(14) inside the beam, and the boundary conditions are given by Eqs. (15)-(20) at the beam ends. The boundary value problem described by Eqs. (13)-(20) is solved employing the Analog Equation Method. According to the analog equation principle, the two coupled differential Eqs. (13)-(14) are substituted by the following analog equations

$$u_{,ss} = q_1(s), \quad w_{,ssss} = q_2(s), \tag{21}, (22)$$

applying the linear differential operators of the 2nd and 4th order respectively to $u = u(s)$ and $w = w(s)$. Both operators have known fundamental solutions. Thus, the solution of the system of Eqs. (13)-(14) can be established by solving the uncoupled system of Eqs. (21), (22) under the same boundary conditions given by Eqs. (15)-(20), provided that the fictitious load distributions q_1, q_2 are first determined. The solution procedure is implemented only numerically by dividing the interval $(0, l)$ into N equal elements on which q_1 and q_2 are assumed constant.

The integral representation of the solution can be written as

$$u(s) = \int_0^l u^*(\xi, s) q_1(\xi) d\xi - [u^* u_{,\xi} - u^*_{,\xi} u]_{\xi=0}^{\xi=l}, \tag{23}$$

$$w(s) = \int_0^l w^*(\xi, s) q_2(\xi) d\xi - [-w^*_{,ssss} w + w^*_{,ss} w_{,\xi\xi} - w^*_{,\xi\xi} w_{,ss} - w^*_{,ss} w_{,\xi\xi} + w^*_{,\xi\xi\xi\xi}]_{\xi=0}^{\xi=l}, \tag{24}$$

where $u^* = u^*(\xi, s)$, $w^* = w^*(\xi, s)$ are the fundamental solutions of the linear differential operators of the 2nd and 4th order respectively, obtained as [61]

$$u^*(\xi, s) = \frac{1}{2}|r|, \tag{25}$$

$$w^*(\xi, s) = \frac{1}{12}(|r|^3 - 3l|r|^2 + 2l^3), \tag{26}$$

where $r = \xi - s$ is the distance between a constant source point at s and ξ runs the interval $[0, l]$. The integral representation of the derivatives of the field functions u, w can be as well derived by immediate differentiation of Eqs. (23) and (24). Moreover, in order to evaluate boundary quantities that are necessary to establish the solution of the problem, the integral representations (23) and (24) are applied to the interval ends $0, l$ as $s \rightarrow s_0 = 0^+, s \rightarrow s_l = l^-$. Thus, the obtained boundary integral equations together with the boundary conditions (15)-(20) permit the establishment of the boundary quantities in terms of the fictitious load.

Since the fictitious loads q_1, q_2 are unknown quantities, a discretization scheme along the interval $[0, l]$ is needed in order to approximate the domain integrals in Eqs. (23) and (24). The interval is divided into N line elements on which the fictitious loads are assumed to vary according to a predefined law (constant, linear, parabolic, etc.). In this work, the case of the constant element assumption is adopted since it combines high accuracy results with simple numerical implementation (see Fig. 2).

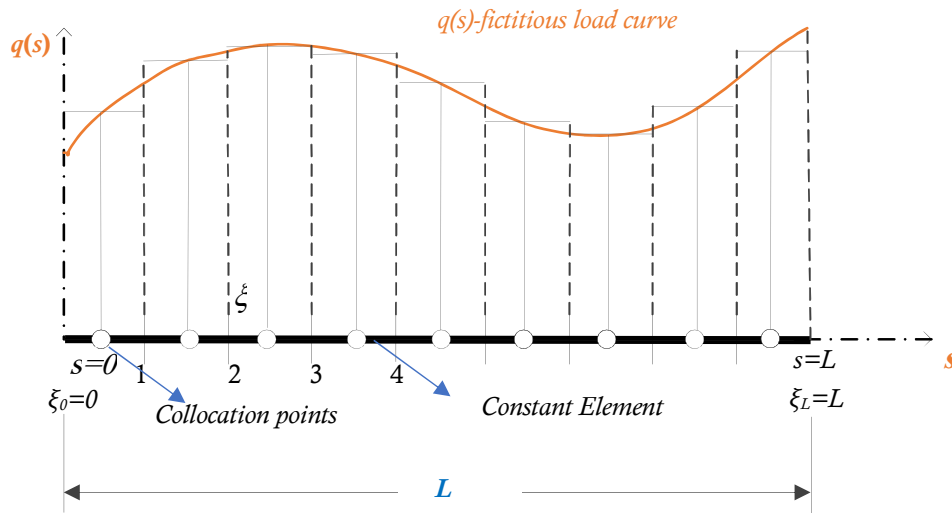


Fig. 2. Constant discretization elements along the interval $[0, l]$ and fictitious load curve.

For a detailed description of the method, the interested reader is referred to the paper of Sapountzakis and Mokos [61]. The final step of the AEM is the collocation of the governing equations (13) and (14) at the N internal nodal points and subsequently the substitution of the values of the field functions u , w and their derivatives. These equations together with the boundary conditions constitute a nonlinear system of $2N + 6$ algebraic equations of $2N + 6$ unknowns, of the form

$$\mathbf{f}(\mathbf{x}) = \mathbf{p}, \quad (27)$$

where $\mathbf{x} = \{\mathbf{q}_1, \mathbf{q}_2, \mathbf{c}\}^T$, and \mathbf{p} is a generalized loading vector. Note that $\mathbf{q}_1, \mathbf{q}_2$ are vectors containing the unknown fictitious loadings at the N nodes, and \mathbf{c} is also a vector containing the six arbitrary integration constants which are determined from the respective boundary conditions.

It should be noted that for a better approximation of the fictitious load distributions q_1 , q_2 , an isogeometric formulation may be a better platform as the underlying basis functions are higher-order [62-64].

3.2 The displacement control algorithm

The nonlinear algebraic system, described by Eq. (27), is solved numerically using the modified Powell's hybrid algorithm [65]. This algorithm is a variation of Newton's method, which uses a finite difference approximation to the Jacobian matrix of the system that corresponds to the generalized stiffness matrix of the problem. The nonlinear equilibrium path of the beam is traced with a load control procedure taking precautions to avoid large step sizes or increasing residuals. The method requires an initial guess of the solution at each load step; $\mathbf{x} = \mathbf{0}$ is used at the first step, while for the next steps, the resolved vector of the previously converged step is employed. The convergence criterion of the algorithm is defined by a tolerance parameter, which in this work is set to 10^{-7} .

However, unstable equilibrium paths are frequently encountered in the nonlinear structural analysis, e.g. due to snap-through and snap-back buckling phenomena. A shallow arch is a typical example of structures that exhibit unstable (snap-through) behavior at a certain level of external vertical loading. In such cases, load control algorithms fail to fully trace the convoluted load-displacement curve when reaching the first limit point, that is the point at which the concavity of the curve changes. To overcome such limit points, a modification to the load control strategy is necessary. This can be achieved by the displacement control algorithm, which uses a dominant displacement component as an independent parameter instead of the usual loading parameter [66]. Although the displacement control algorithm copes very well in problems with snap-through buckling, for more complex problems that exhibit snap-back behaviors recourse to the cylindrical arc-length control algorithm is inevitable.

In the displacement control algorithm, a displacement component is selected at one of the structure's degrees of freedom and is incremented by a prescribed amount Δu_{ctrl} at each load step. Consequently, an extra restraining equation is added to the nonlinear system of Eqs. (27) of the form

$$x_{\text{ctrl}} + u_{\text{ctrl}} = 0, \quad (28)$$

where x_{ctrl} is the component of the unknown vector \mathbf{x} that corresponds to the selected degree of freedom and u_{ctrl} is the imposed known value of the displacement at each step. In turn, the load vector is considered as an unknown variable and must be adjusted within the load step so as the selected displacement takes the prescribed value. Taking into account these considerations, the system of Eqs. (27) together with E. (28) comprise a nonlinear system of $2N + 7$ equations

with $2N + 7$ unknowns that can be written as

$$\mathbf{g}(\mathbf{x}, \lambda) = \mathbf{0}, \tag{29}$$

where λ is the parameter that multiplies the loading vector. Further, an incremental procedure is commenced for the solution of the nonlinear system described by Eq. (29) starting with an initial guess of the vector \mathbf{x} and the loading parameter λ . Next, for the first increment of u_{ctrl} the system is solved with the modified Powell’s hybrid algorithm. The obtained solution (\mathbf{x}, λ) is considered as an initial guess for the next increment of u_{ctrl} and the procedure starts over again and continues up to either the analyst’s desired value u_{ctrl} or the failure of the structure. The solution of the system provides the values of the fictitious loads q_1, q_2 as well as the values of the field functions u, w and their derivatives at the N internal nodal points.

3.3 The Layered Analysis

The previous analysis applies when the stress resultants N and M can be expressed as continuous functions one and two times differentiable in terms of s , respectively, as in Eqs. (8), (9). In such cases, they can be analytically differentiated with respect to s and the governing equations can be obtained directly in terms of the displacements in Eqs. (13), (14). However, this is not always possible since the constitutive law of the material is not always a priori known, or even cannot be expressed by a mathematical function but only by sets of experimental data. When this is the case, an alternative method of integration over the cross-section must be adopted in order N and M can be determined. Further, an appropriate numerical scheme must be established for the differentiation of the stress resultants in terms of s and the satisfaction of the governing Eqs. (11), (12). To this end, a layered approach [52] is employed for the integration over the cross-section in conjunction with the AEM for the differentiation along the beam length. The fiber/layered approach has found numerous applications on various engineering problems, such as, a fiber-based nonlinear Euler-Bernoulli beam modeling to capture the plasticity growth in large-deformation frames [63], snap-through instability behaviors of structures that exhibit temperature-dependent material response [67], a higher-order gradient damage model [68]. In principle, the layered analysis comprises two distinct discretization steps. First, the beam length is divided into a number of monitoring cross-sections. The position of each cross-section coincides with the nodal points of the longitudinal discretization and the two ends of the beam. Second, each cross-section is decomposed into a number of layers of constant height. It is assumed that within each layer Eqs. (2), (3) hold for the nonlinear strain-displacement relation (see Fig. 3). Consequently, strains are expressed in terms of the nodal displacement component at the center of the layer. Next, given the strain-displacement expressions, stresses can be determined, and the stress resultants can be evaluated with a numerical integration scheme. The discretization scheme is depicted in Fig. 3.

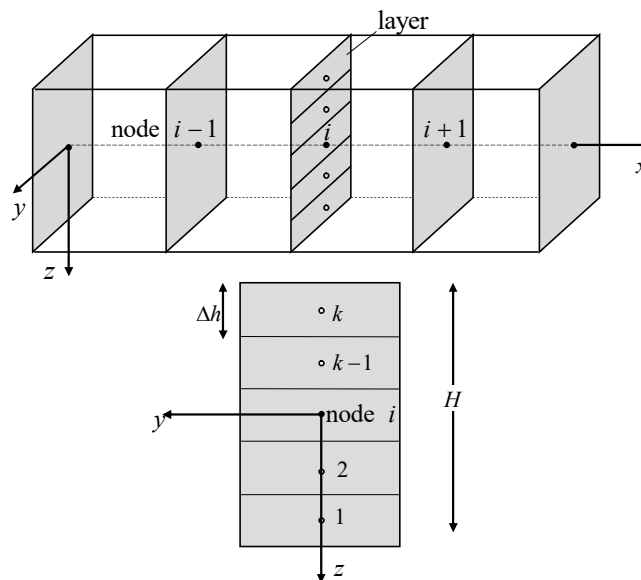


Fig. 3. Discretization of the beam into monitoring cross-sections, cross-section layers, and strain distribution.

An odd number of layers k is selected so the center of the beam’s cross-section is located at the middle of the $(k + 1) / 2$ layer. The constant height of the layers is Δh . The z coordinate of the center of the i -th layer is written as

$$z_i = \left(\frac{k + 1}{2} - i \right) \Delta h. \tag{30}$$

The axial force N_i and the bending moment M_i for each layer can be computed as



$$N_i = \sigma^i \Delta A_i, \quad M_i = \sigma^i z_i \Delta A_i, \quad (31), (32)$$

where $\sigma^i = f(\varepsilon^i)$ are the stress component at the center of each layer and ΔA_i the area of each layer. Therefore, the stress resultants can be approximated as

$$N = \sum_{i=0}^k \sigma^i \Delta A_i, \quad M = \sum_{i=0}^k \sigma^i z_i \Delta A_i. \quad (33), (34)$$

After the determination of the axial force and the bending moment at each node, their derivatives are evaluated numerically using a method thoroughly described in [69]. Having established the numerical expressions of the stress resultants and their derivatives in terms of the unknown nodal displacements, the nonlinear Eqs. (11) and (12) together with the boundary conditions given in Eqs. (15)-(20) are solved employing the displacement control algorithm described previously. The employed subroutine that solves the system of the nonlinear equations by implementing the displacement control algorithm is called directly by the main program and is described by the pseudocode compiled in Table 1.

Table 1. Pseudocode of the nonlinear solver with displacement control.

Initialize displacement control method variables (displacement increment step and error tolerance)

Initialize the solution vector \mathbf{x}_{guess} and the loading parameter λ_0 .

for a defined number of iterations j

$u_{ctrl} = j \Delta u_{ctrl}$

call the subroutine that solves the system of nonlinear equations (modified Powell hybrid algorithm and finite-difference approximation to the Jacobian) and provides the solution (\mathbf{x}, λ)

update the solution vector and the loading parameter

$\mathbf{x}_{guess} = \mathbf{x}$

for the number of nodes N of the longitudinal discretization i

calculate displacements and their derivatives at each node

for a defined number of layers of the cross-section discretization k

calculate strains and stresses (according to constitutive laws of SMAs later described) and stress resultants on each cross-sectional layer

calculate stress resultants for the whole cross-section of a curved nonlinear beam

end for

end for

end for

4. Stress-strain Constitutive Equation

In view of the above-described methodology, a stress-strain experimental curve of the following polynomial form is employed in the layered analysis loop (Table 1):

$$\sigma(s, z) = \alpha_1 \varepsilon + \alpha_2 \varepsilon^2 + \alpha_3 \varepsilon^3 + \alpha_4 \varepsilon^4 + \alpha_5 \varepsilon^5 \quad (35)$$

where $\alpha_1, \alpha_2, \alpha_3, \alpha_4$ and α_5 are constants derived by the least-squares method and the corresponding experimental curve. Their values can differ depending on the experimental data employed. The fitted stress-strain curves studied in this work are reported by Shang and Wang [32] and Tsiatas et al. [52].

In [32] the superelastic TiNi shape memory alloy bars provided by Xi'an Saite Metal Materials Development Co., Ltd served as experimental materials. The chemical compositions of SMA materials were Ti-55.86 wt% (weight percent) Ni, the phase transformation temperatures were $M_f = -53$ °C, $M_s = -33$ °C, $A_s = -25$ °C, $A_f = -5$ °C, the diameter of the experimental bars was 2.5 mm, and the phase composition at room temperature was austenite. In this case, the polynomial form of the stress-strain curve is

$$\sigma(s, z) = 70000\varepsilon - 2.8 \times 10^6 \varepsilon^2 + 4.474 \times 10^7 \varepsilon^3 - 2.1001 \times 10^8 \varepsilon^4 - 1.419 \times 10^8 \varepsilon^5 \quad (36)$$

In [52] the SMA's stress-strain relation obtained by interpolating the experimental curve presented in [70] for the Zhang and Zhu [71] testing program. The wire testing program involved superelastic nitinol wires with a diameter of 0.58 mm,

acquired from Memry Corporation. These cold-drawn nitinol wires had a composition to exhibit superelastic behavior. The ultimate tensile strength of the tested nitinol wires was 1400 MPa. The uniaxial tension test of the superelastic nitinol wires was carried out using an MTS servohydraulic test machine at room temperature of 23 °C, and the gage length of the wire test specimens was 254 mm (10 inches) [59]. In this case, the polynomial form of the stress-strain curve is

$$\sigma(s, z) = 43308.4\varepsilon - 1.84007 \times 10^6 \varepsilon^2 + 3.8728 \times 10^7 \varepsilon^3 - 3.49169 \times 10^8 \varepsilon^4 + 1.15776 \times 10^9 \varepsilon^5 \quad (37)$$

The stress-strain curves of the two models are shown in Fig. 4a. It is obvious that the model of Shang and Wang [32] exhibits a stiffer response, namely a higher restoring force, as compared to that of Tsiatas et al. [52]. However, the shape of both curves exhibits common features.

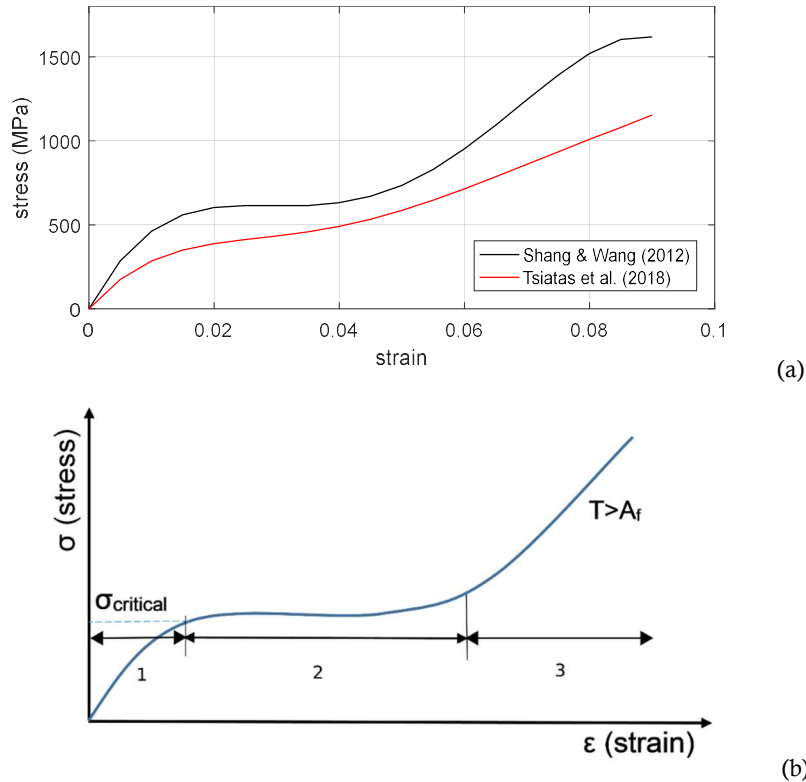


Fig. 4. Stress-strain curve of SMA

In general, the curves are divided into three regions during loading (see Fig. 4b). The first one which accounts for the almost linear part before the critical stress σ_{critical} has been reached, the second one which describes the phase transformation of the material to martensite (associated with a reduced modulus of elasticity) and the third region which accounts again for a linear behavior but of a stiffer material with different modulus of elasticity. The ambient temperature is constant and higher than the temperature at which the microstructure of the material is fully austenitic (A_f). Thus, the initial austenite is loaded elastically (first region of the superelastic curve) up to the critical stress after which the transformation to martensite initiates (second region of the curve). Afterward, the martensitic volume fraction is gradually increased in the microstructure until it becomes dominant. When the loading is increased further, the created fully martensite is elastically deformed with a Young modulus smaller than the one of the elastic initial austenitic phases, but still significantly higher than the modulus during the transformation phase.

The considered polynomial curves can accurately describe this behavior and can be simply integrated into the solution algorithm for the proposed numerical procedure presented illustrated by the flowchart in Fig. 5.

5. Numerical Examples

Based on the numerical procedure presented in the previous sections, a computer program has been developed, and representative examples have been studied in order to demonstrate the efficiency and accuracy of the proposed method. It is noted that the numerical results have been obtained with up to 71 nodal points (longitudinal discretization) and up to 21 layers (cross-sectional discretization) unless otherwise stated. However, it should be noted that satisfactory convergence and accuracy could also be achieved with a coarser discretization.

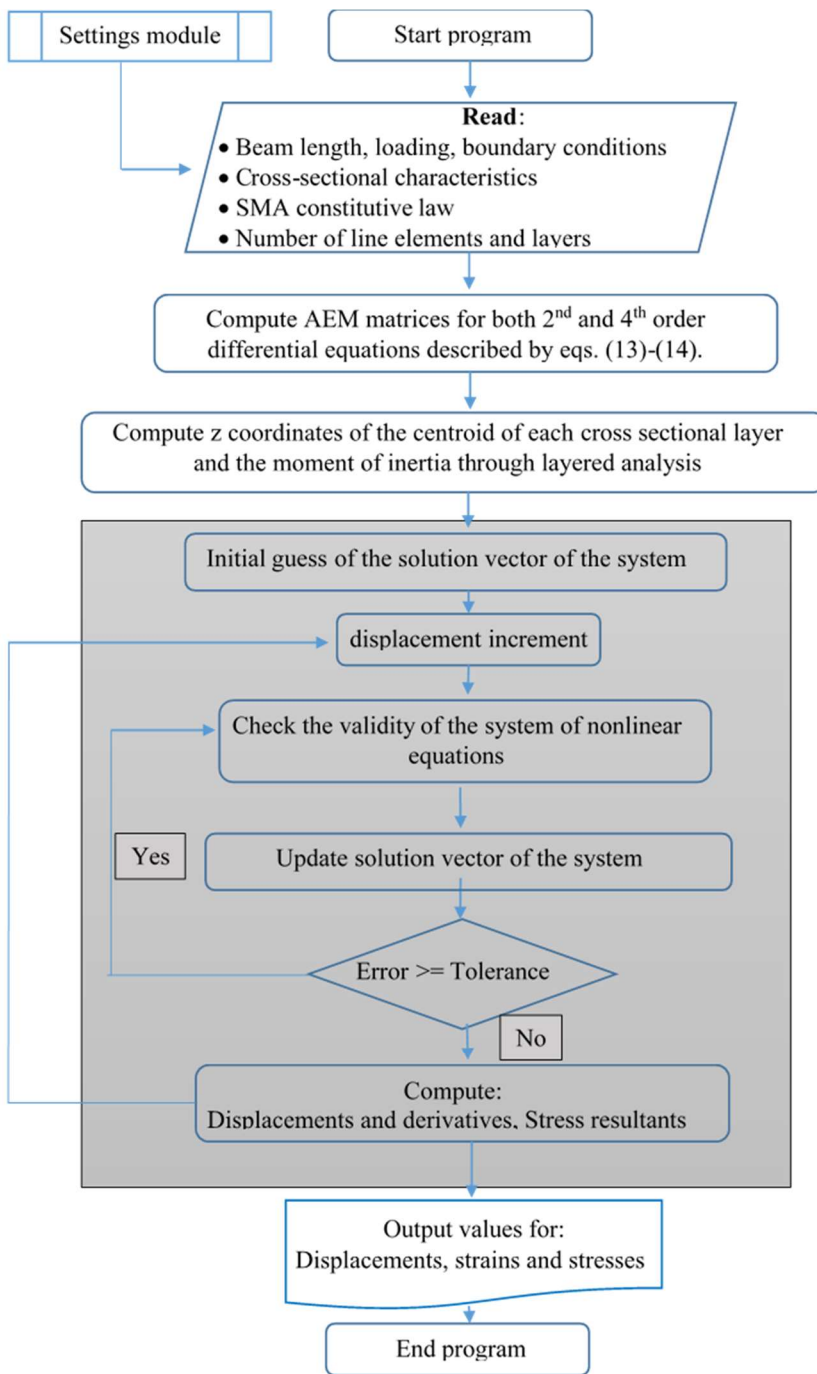


Fig. 5. A flowchart of the solution algorithm for the determination of displacements, strains, and stresses in an SMA arch

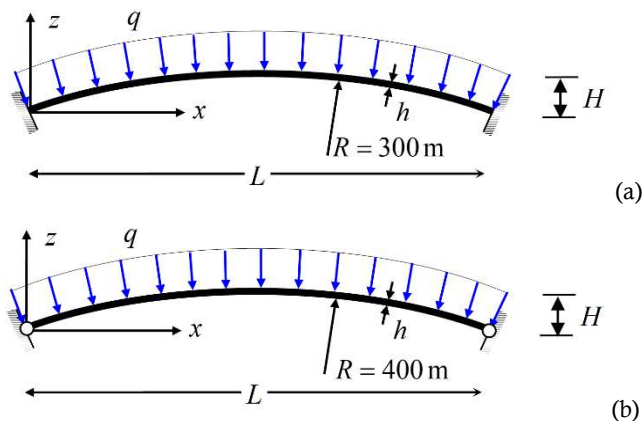


Fig. 6. Shallow arches geometrical characteristics of Example 5.1

Example 1: Steel shallow arch

In the first example, we study the nonlinear response of both fixed (Fig. 6a) and pin-ended (Fig. 6b) steel shallow arches subjected to a compressive distributed load in the radial direction. The arch has a uniform rectangular cross-section $b \times h$. The data employed are: $L = 34.0\text{ m}$, $b = 1.0\text{ m}$, $h = 0.3\text{ m}$, and $E = 200 \times 10^6\text{ kN/m}^2$. The results are obtained using 121 elements and 21 layers.

To compare the results obtained from the presented layered formulation, the arches are also analyzed using the numerical method presented by Tsiatas and Babouskos [53], who employed an analytical cross-sectional integration for the evaluation of the stress resultants. In this case, all the results were obtained using $N = 121$ elements. The results for the central displacement obtained by the two numerical methods are presented in Table 2. It can be concluded that for both fixed and pin-ended shallow arches the results show a very good agreement.

Table 2. Central displacement for both fixed and pin-ended shallow arches in example 5.1

w (m)	q (kN/m)		w (m)	q (kN/m)	
	Analytical integration	Layered approach		Analytical integration	Layered approach
fixed arch			pin-ended arch		
0.100	35.529	35.532	0.090	16.574	16.574
0.196	50.120	50.124	0.181	21.360	21.364
0.291	53.223	53.234	0.271	18.502	18.513
0.387	51.280	51.302	0.361	11.626	11.645
0.482	49.350	49.343	0.452	3.902	3.921
0.582	51.583	51.578	0.542	-1.340	-1.337
0.678	61.333	61.317	0.723	13.165	13.073
0.773	82.281	82.148	0.803	38.572	38.406

First, the curves of the load versus normalized central displacement of the fixed arch are shown in Fig. 7, for the two methods. A snap-through buckling occurs when the external load becomes greater than $q_{cr} = 53.24\text{ kN/m}$. The result is also verified using the approximating relation (78) for the symmetric buckling load of fixed arches, presented in [72], which gives 51.97 kN for modified slenderness $\lambda_s = l^2 / 4R\sqrt{I/A} = 11.14$.

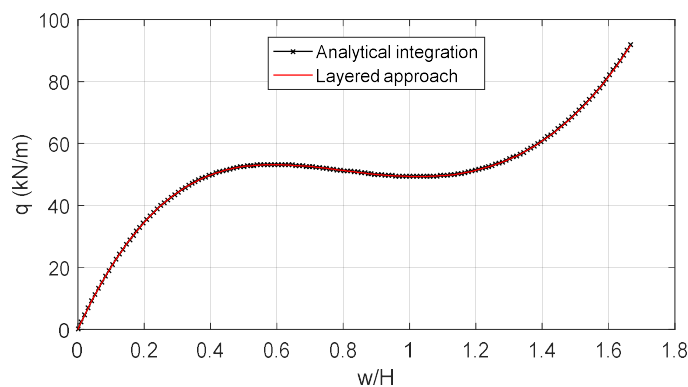


Fig. 7. Load versus normalized central displacement curves of the fixed arch in example 5.1.

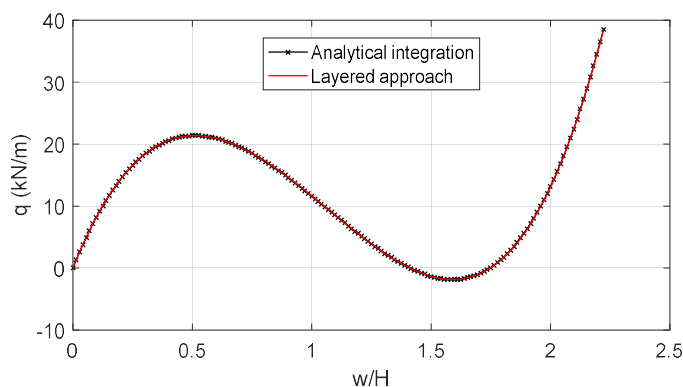


Fig. 8. Load versus normalized central displacement curves of the pin-ended arch in example 5.1.

Second, the curves of the load versus normalized central displacement of the pin-ended arch are shown in Fig. 8, for the two methods. A snap-through buckling also appears when the external load becomes greater than $q_{cr} = 21.37 \text{ kN/m}$. The result is again verified using the approximating relation (59) for the symmetric buckling load of pin-ended arches, presented in [72], which gives 21.81 kN for the different modified slenderness $\lambda_s = l^2 / 4R\sqrt{I/A} = 8.35$.

Example 2: SMA shallow arch for two load types

In this second example, the nonlinear response of fixed and pin-ended shallow arches made of SMA is studied. The arch is separately examined for a compressive distributed load in the radial direction and for a concentrated vertical load at the midspan. The arch has a uniform rectangular cross-section $b \times h$. The data employed are: $L = 0.5 \text{ m}$, $b = h = 0.01 \text{ m}$ and $R = 0.35 \text{ m}$. Considering the constitutive law of the SMA, the two models presented in section 4 are examined.

Firstly, the behavior of the shallow arch under a radial uniformly distributed load is examined. The analysis is performed for fixed and pin-ended boundary conditions for each polynomial curve and the nonlinear curves of load versus normal displacement at the center of the arch are depicted in Fig. 9. Next, the shallow arch is subjected to a concentrated load at the midspan, and the corresponding nonlinear curves are shown in Fig. 10.

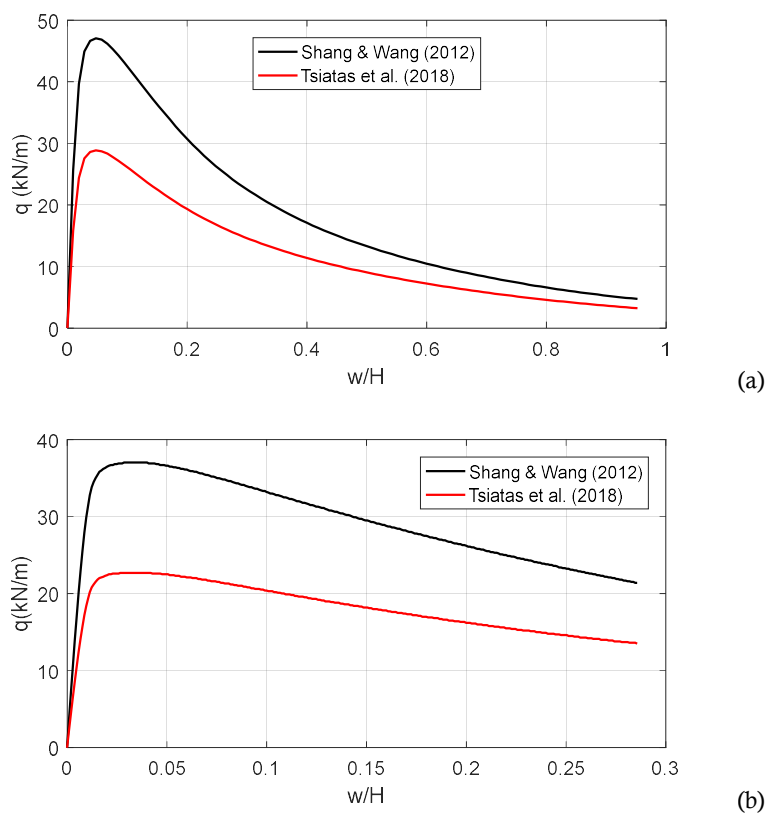


Fig. 9. Uniformly distributed load versus normalized central displacement curves of the (a) fixed and (b) pin-ended arch in example 5.2.

It is noteworthy that the buckling load differs significantly for both SMA models. As was expected the stiffer model of Shang and Wang [32] exhibits larger buckling loads compared to that of Tsiatas et al. [52] for the two types of boundary conditions. However, for both models, the post-buckling behavior presents similar characteristics. Moreover, from the obtained results it can be deduced that the influence of the boundary conditions on the buckling and post-buckling is significant. For both load types, the fixed arch manifests larger buckling loads compared to the pin-ended arch. Note that, the presented results are limited to the common displacement range of the two models, which is usually controlled by the Tsiatas et al. [52] model.

Finally, in Figs. 11 and 12 the profiles of the axial force and the bending moment are presented for both SMA models and for both types of boundary conditions for distributed loading. It must be noted that all the curves refer to the respective critical state for each case, namely when the load is equal to the buckling load.

The main conclusion drawn by this example is that there is no unique constitutive law describing the superelastic behavior of the SMA material. The stress-strain constitutive curve depends on a variety of parameters including the chemical composition of the alloy, and geometrical and training effects, to name only a few. As so, an experimental test should always precede any numerical modeling.

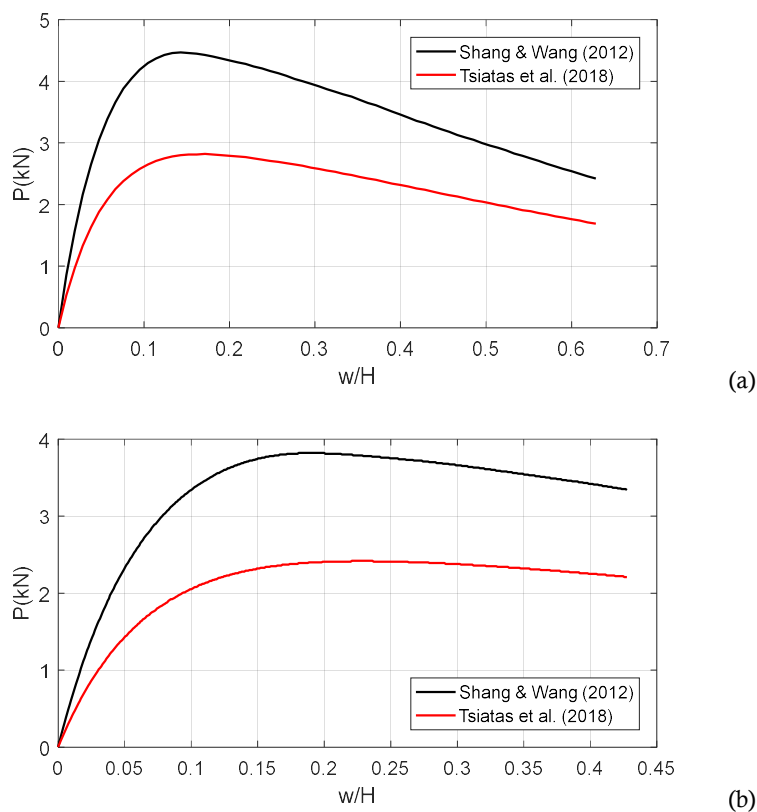


Fig. 10. Concentrated load versus normalized central displacement curves of the (a) fixed arch and (b) pin-ended arch in example 5.2.

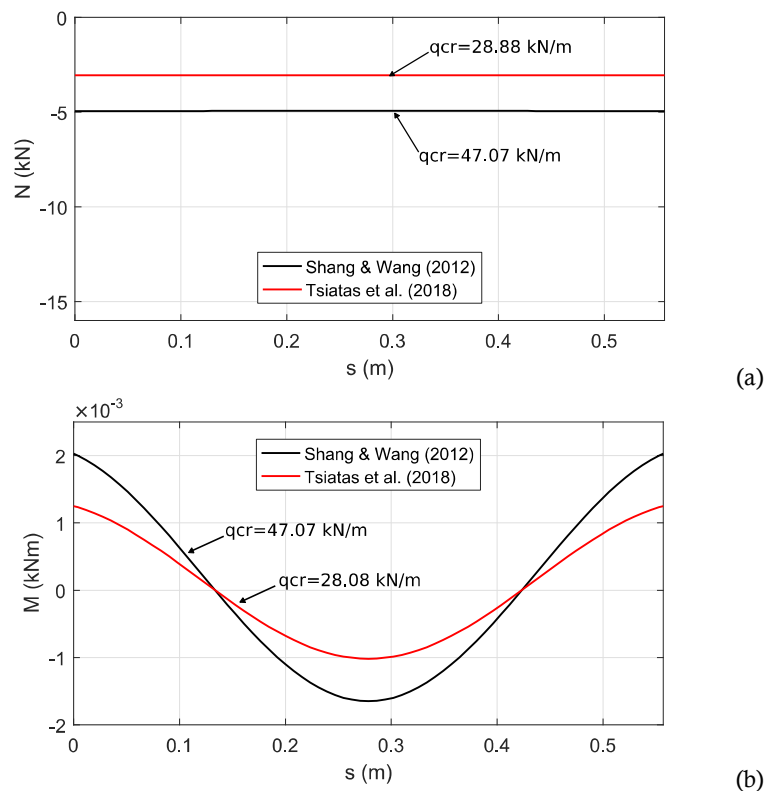


Fig. 11. Profile of the (a) axial force and (b) bending moment of the fixed arch under uniformly distributed load in example 5.2.

Example 3: SMA shallow arch for three modified slenderness ratios

In this third example, the influence of the modified slenderness $\lambda_s = l^2 / (4R\sqrt{I/A})$ to the nonlinear response of fixed and pin-ended shallow arches made of SMA is investigated. Two separate load types are considered, a compressive distributed load in the radial direction and a concentrated vertical load at the midspan. The arch has the geometrical



characteristics of the previous second example, whereas three values of radius of curvature are considered, namely $R = 0.35\text{ m}$, $R = 0.40\text{ m}$, and $R = 0.45\text{ m}$ with respective values of modified slenderness $\lambda_s = 76.75$, $\lambda_s = 63.16$, and $\lambda_s = 54.09$. The SMA is described by the stress-strain relation presented by Shang and Wang [32] which is more suitable for a beam. In Figs. 13 and 14, the nonlinear curves of uniformly distributed and concentrated load versus normal displacement at the center of the arch are shown for the two types of boundary conditions and the three modified slenderness ratios. For all the examined arches it is revealed that the greater the modified slenderness ratio, the greater the critical load.

Table 3. Uniformly distributed and concentrated buckling loads for the three values of modified slenderness for both fixed and pin-ended shallow arches in example 5.3

Modified slenderness ratio λ_s	uniformly distributed load (kN/m)		concentrated load (kN)	
	fixed	pin-ended	fixed	pin-ended
54.09	37.419	30.951	4.097	3.577
63.16	42.018	33.980	4.302	3.718
76.75	47.070	37.024	4.467	3.818

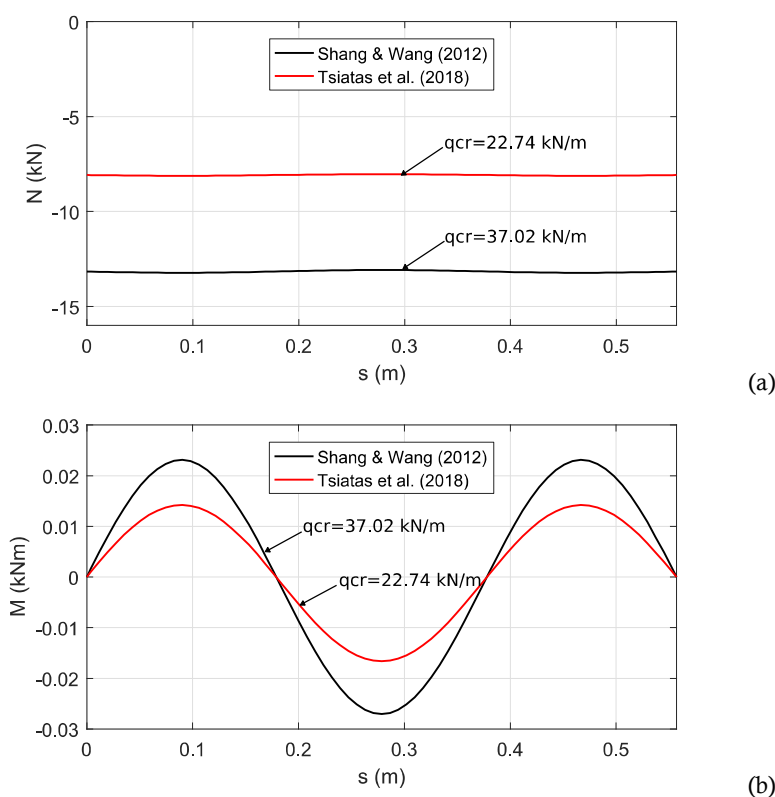


Fig. 12. Profile of the (a) axial force and (b) bending moment of the pin-ended arch under uniformly distributed load in example 5.2.

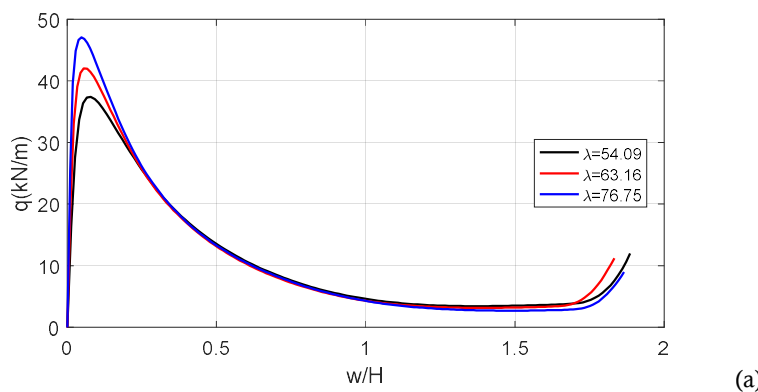


Fig. 13. Uniformly distributed load versus normalized central displacement curves of the (a) fixed and (b) pin-ended arch for several values of modified slenderness in example 5.3.

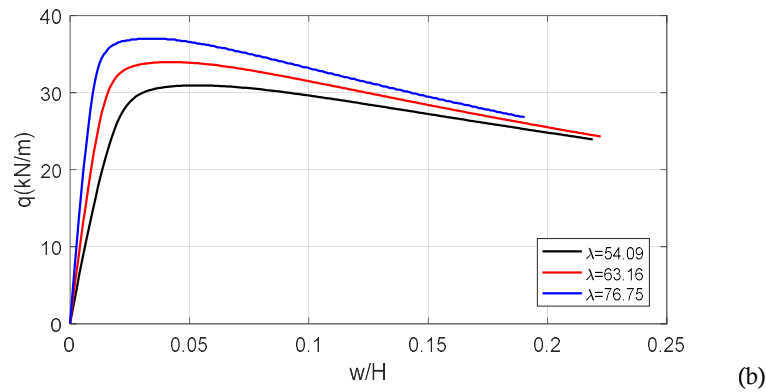


Fig. 13. Continued.

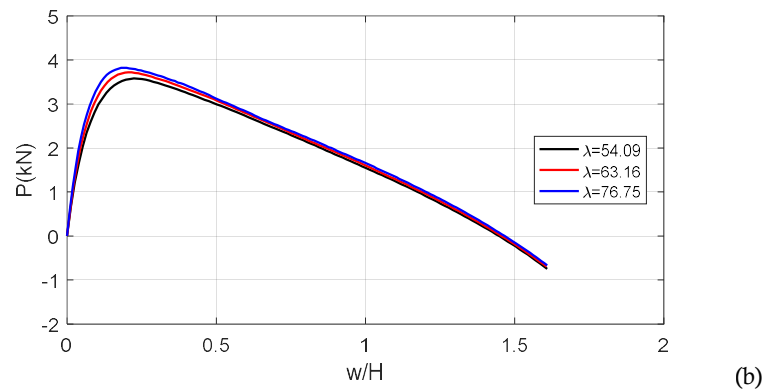
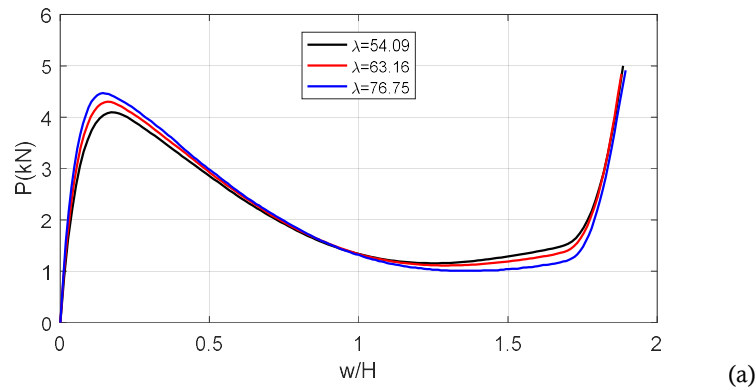


Fig. 14. Concentrated load versus normalized central displacement curves of the (a) fixed and (b) pin-ended arch for several values of modified slenderness in example 5.3.

Comparing the post-buckling response of the concentrated load case for the two types of boundary conditions (see Fig. 14a and 14b), the pin-ended arch exhibits a completely different behavior compared to that of the fixed arch since the load-carrying capacity decreases rapidly after the buckling. Moreover, the fixed arch under concentrated load (see Fig. 14a) exhibits a “snap-through type” buckling in contrast to the fixed arch under uniform load (see Fig. 13a). This happens because in the former case (Fig. 14a) the maximum strain emerges in the third region of the stress-strain curve (see section 4) which accounts for a linear stiffening behavior with a higher modulus of elasticity. Lastly, in Table 3 the critical loads of the analyzed arches are presented for all types of boundary conditions, modified slenderness ratios, and load types.

6. Conclusions

In this paper, the nonlinear buckling and post-buckling behavior of shallow arches made of Shape Memory Alloy (SMA) was investigated. In order to introduce the SMA constitutive law, the stress-strain experimental curves described in the literature were employed together with a fiber approach at specific control cross-sections along the beam. The numerical solution of the longitudinal problem was achieved using the Analog Equation Method, together with an iterative procedure which was based on a Newton-Raphson scheme and a displacement control algorithm. Several representative examples were studied, validating the assumptions made for the proposed model and the solution algorithm. The essential features and novel aspects of the present formulation are summarized as follows:

- Numerical results for the nonlinear buckling load of SMA shallow arches are reported for the first time in the literature.



- The employed solution method exhibits stability and a small number of constant elements are adequate to obtain accurate results for the displacements and the stress resultants.
- A new displacement control algorithm is used for the solution of the nonlinear system of equations. This method allows following the nonlinear equilibrium path and overcomes successfully bifurcation and limit points.
- Although this displacement control algorithm copes very well in problems with snap-through buckling, for more complex problems that exhibit snap-back behaviors recourse to the cylindrical arc-length control algorithm is inevitable. This is, however, the subject of future research.
- The proposed method can handle any SMA stress-strain relation (derived by an experimental curve) in the formulation of the nonlinear deformation differential equations.
- There is no unique constitutive law describing the superelastic behavior of the SMA material. As so, an experimental test should always precede any numerical modeling.
- In general, the buckling load differs significantly for both examined SMA models, and the influence of the boundary conditions on the buckling and post-buckling is pronounced. However, for both models, the post-buckling behavior presents similar characteristics.
- As the radius of the arches increases, the modified slenderness ratio decreases. From all the examined arches it is revealed that the greater the modified slenderness ratio, the greater the critical load.
- The pin-ended SMA arch exhibits a completely different behavior compared to that of the fixed arch since the load-carrying capacity decreases rapidly after the buckling.

Author Contributions

All authors made a substantial, direct and intellectual contribution to this work. The manuscript was written through the contribution of all authors. All authors discussed the results, reviewed and approved the final version of the manuscript.

Conflict of Interest

The authors declared no potential conflicts of interest with respect to the research, authorship, and publication of this article.

Funding

This research is implemented through the Operational Program "Human Resources Development, Education and Lifelong Learning" and is co-financed by the European Union (European Social Fund) and Greek national funds.



Ευρωπαϊκή Ένωση
Ευρωπαϊκό Κοινωνικό Ταμείο

Επιχειρησιακό Πρόγραμμα
Ανάπτυξη Ανθρώπινου Δυναμικού,
Εκπαίδευση και Διά Βίου Μάθηση
Ειδική Υπηρεσία Διαχείρισης
Με τη συγχρηματοδότηση της Ελλάδας και της Ευρωπαϊκής Ένωσης



References

- [1] Song, G., Ma, N, Li, H.N.: Applications of Shape Memory Alloys in Civil Structures, *Engineering Structures*, 28, 2006, 1266–1274.
- [2] Vieta, N.V., Zakia, W., Umer, R., Analytical Model of Functionally Graded Material/Shape Memory Alloy Composite Cantilever Beam Under Bending, *Composite Structures*, 203, 2018, 764-776.
- [3] Levitas, V.I., Roy, A.M., Preston, D.L., Multiple twinning and variant-variant transformations in martensite: Phase-field approach, *Physical Review B*, 88, 2013, 054113.
- [4] Levitas, V.I., Roy, A.M., Multiphase phase field theory for temperature- and stress-induced phase transformations, *Physical Review B*, 91, 2015, 174109.
- [5] Levitas, V.I., Roy, A.M., Multiphase phase field theory for temperature-induced phase transformations: Formulation and application to interfacial phases, *Acta Materialia*, 105, 2016, 244-257.
- [6] Lagoudas, D.C. (ed), *Shape Memory Alloys modeling and Engineering Applications*, Springer, New York, 2008.
- [7] Tanaka, K., A Thermomechanical Sketch of Shape Memory Effect: One-Dimensional Tensile Behavior, *Res Mechanica*, 18, 1986, 251-263.
- [8] Liang, C., Rogers, C.A., One-Dimensional Thermomechanical Constitutive Relations for Shape Memory Materials, *Journal of Intelligent Material Systems and Structures*, 8, 1997, 285-302.
- [9] Auricchio, F., Sacco, E., A One-Dimensional Model for Superelastic Shape-Memory Alloys with Different Elastic Properties Between Austenite and Martensite, *International Journal of Non-Linear Mechanics*, 32(6), 1997, 1101-1114.
- [10] Auricchio, F., Sacco, E., A Superelastic Shape-Memory-Alloy Beam Model, *Journal of Intelligent Material Systems and Structures*, 8, 1997, 489-501.
- [11] Auricchio, F., Taylor, R.L., Lubliner, J., Shape Memory Alloys: Macromodelling and Numerical Simulations of the Superelastic Behavior, *Computer Methods in Applied Mechanics and Engineering*, 146, 1997, 281-312.

- [12] Mori, T., Tanaka, K., Average Stress in Matrix and Average Elastic Energy of Materials with Misfitting Inclusions, *Acta Metallurgica*, 21, 1973, 571-574.
- [13] Brinson, L.C., One-Dimensional Constitutive Behavior of Shape Memory Alloys: Thermo-Mechanical Derivation with Non-Constant Material Functions and Redefined Martensite Internal Variable, *Journal of Intelligent Materials Systems and Structures*, 4, 1993, 229-242.
- [14] Souza, A.C., Mamiya, E.N., Zouain, N., Three-Dimensional Model for Solids Undergoing Stress-Induced Phase Transformations, *European Journal of Mechanics-A/ Solids*, 17, 1998, 789-806.
- [15] Auricchio, F., Petrini, L., A Three-Dimensional Model Describing Stress-Temperature Induced Solid Phase Transformations. Part I: Solution Algorithm and Boundary Value Problems, *International Journal for Numerical Methods in Engineering*, 61, 2004, 807-836.
- [16] Ghomshei, M.M., Tabandeh, N., Ghazavi, A., Gordaninejad, F., Nonlinear Transient Response of a Thick Composite Beam with Shape Memory Alloy Layers, *Composites Part B: Engineering*, 36, 2005, 9-24.
- [17] Khalili, S.M.R., Botshekanan Dehkordi, M., Carrera, E., Shariyat, M., Non-Linear Dynamic Analysis of a Sandwich Beam with Pseudoelastic SMA Hybrid Composite Faces Based on Higher Order Finite Element Theory, *Composite Structures*, 96, 2013, 243-255.
- [18] Ostadrahimi, A., Arghavani, J., Poorasadion, S., An Analytical Study on the Bending of Prismatic SMA Beams, *Smart Materials and Structures*, 24, 2015, 125035.
- [19] Razavilar, R., Fathi, A., Dardel, M., Arghavani Hadi, J., Dynamic Analysis of a Shape Memory Alloy Beam with Pseudoelastic Behavior, *Journal of Intelligent Material Systems and Structures*, 29(9), 2018, 1835-1849.
- [20] Fahimi, P., Eskandari, A.H., Baghani, M., Taheri, A., A Semi-Analytical Solution for Bending Response of SMA Composite Beams Considering SMA Asymmetric Behavior, *Composites Part B*, 163, 2019, 622-633.
- [21] Chung, J. H., Heo, J.S., Lee, J.J., Implementation Strategy for the Dual Transformation Region in the Brinson SMA Constitutive Model, *Smart Materials and Structures*, 16, 2006, N1-N5.
- [22] DeCastro, J.A., Melcher, K.J., Noebe, R.D., Gaydosh, D.J., Development of a Numerical Model for High-Temperature Shape Memory Alloys, *Smart Materials and Structures*, 16, 2007, 2080-2090.
- [23] Khandelwal, A., Buravalla, V.R., A Correction to the Brinson's Evolution Kinetics for Shape Memory Alloys, *Journal of Intelligent Materials Systems and Structures*, 19(1), 2008, 43-46.
- [24] Poorasadion, S., Arghavani, J., Naghdabadi, R., Sohrabpour, S., An Improvement on the Brinson Model for Shape Memory Alloys with Application to Two-Dimensional Beam Element. *Journal of Intelligent Materials Systems and Structures*, 25(15), 2013, 1905-1920.
- [25] Auricchio, F., Reali, A., Stefanelli, U., A Macroscopic 1D Model for Shape Memory Alloys Including Asymmetric Behaviors and Transformation-Dependent Elastic Properties, *Computer Methods in Applied Mechanics and Engineering*, 198, 2009, 1631-1637.
- [26] Mirzaeifar, R., DesRoches, R., Yavari, A., Gal, K., On Super-Elastic Bending of Shape Memory Alloy Beam, *International Journal of Solids and Structures*, 50(10), 2013, 1664-1680.
- [27] Zaki, W., Moumni, Z., A Three-Dimensional Model of the Thermomechanical Behavior of Shape Memory Alloys, *Journal of the Mechanics and Physics of Solids*, 55, 2007, 2455-2490.
- [28] Zaki, W., Moumni, Z., Morin, C., Modeling Tensile-Compressive Asymmetry for Superelastic Shape Memory Alloys, *Mechanics of Advanced Materials and Structures*, 18(7), 2011, 559-564.
- [29] Viet, N.K., Zaki, W., Umer, R., Analytical Model for a Superelastic Timoshenko Shape Memory Alloy Beam Subjected to a Loading-Unloading Cycle, *Journal of Intelligent Material Systems and Structures*, 29(20), 2018, 3902-3922.
- [30] Rejzner, J., Lexcellent, C., Raniecki, B., Pseudoelastic Behavior of Shape Memory Alloy Beams under Pure Bending: Experiment and Modelling, *International Journal of Mechanical Sciences*, 44, 2002, 665-86.
- [31] Watkins, R.T., Reedlunn, B., Daly, S., Shaw, J.A., Uniaxial, Pure Bending, and Column Buckling Experiments on Superelastic Niti Rods and Tubes, *International Journal of Solids and Structures*, 146, 2018, 1-28.
- [32] Shang, Z., Wang, Z., Nonlinear Tension-Bending Deformation of a Shape Memory Alloy Rod, *Smart Materials and Structures*, 21, 2012, 115004.
- [33] Atanackovic, T., Achenbach, M. Moment curvature relations for a pseudoelastic beam, *Continuum Mechanics and Thermodynamics*, 1, 1989, 73-80.
- [34] Mirzaeifara, R., DesRoches, R., Yavarib A., Gall, K., A Closed-form Solution for Superelastic Shape Memory Alloy Beams Subjected to Bending, *Proc. SPIE 8342, Behavior and Mechanics of Multifunctional Materials and Composites*, 83421O, 2012.
- [35] Sepiani, H., Ebrahimi, F., Karimipour, H., A mathematical model for smart functionally graded beam integrated with shape memory alloy actuators, *Journal of Mechanical Science and Technology*, 23, 2009, 3179-3190.
- [36] Bingfei, L., Dui, G., Yang, S., On the transformation behavior of functionally graded SMA composites subjected to thermal loading, *European Journal of Mechanics - A/Solids*, 40, 2013, 139-147.
- [37] Marfa, S., Sacco, E., Reddy, J.N., Superelastic and shape memory effects in laminated shape-memory-alloy beams, *AIAA Journal*, 41(1), 2003, 100-109.
- [38] Viet, N.V., Zaki, W., Umer, R., Bending models for superelastic shape memory alloy laminated composite cantilever beams with elastic core layer, *Composites: Part B*, 147, 2018, 86-103.
- [39] Bodaghi, M., Damanpack, A.R., Aghdam, M.M., Shakeri, M., Active shape/stress control of shape memory alloy

laminated beams, *Composites: Part B*, 56, 2014, 889-899.

[40] Bayat, Y., Ekhteraei Toussi, H., Analytical layerwise solution of nonlinear thermal instability of SMA hybrid composite beam under nonuniform temperature condition, *Mechanics of Advanced Materials and Structures*, 2019, 1-14 (in press).

[41] Babaee, A., Sadighi, M., Nikbakht, A., Alimirzaei, S., Generalized differential quadrature nonlinear buckling analysis of smart SMA/FG laminated beam resting on nonlinear elastic medium under thermal loading, *Journal of Thermal Stresses*, 41(5), 2018, 583-607.

[42] Akbaş, S.D., Post-Buckling Analysis of Axially Functionally Graded Three-Dimensional Beams, *International Journal of Applied Mechanics*, 7(3), 2015, 1550047.

[43] Torki, M.E., Reddy, J.N., Buckling of Functionally Graded Beams with Partially Delaminated Piezoelectric Layers, *International Journal of Structural Stability and Dynamics*, 16(3), 2016, 1450104.

[44] Anish, Chaubey, A., Kumar, A., Kwiatkowski, B., Barnat-Hunek, D., Widomski, M.K., Bi-Axial Buckling of Laminated Composite Plates Including Cutout and Additional Mass, *Materials*, 12(11), 2019, 1750.

[45] Kaveh, A., Dadras, A., Malek, N.G., Buckling load of laminated composite plates using three variants of the biogeography-based optimization algorithm, *Acta Mechanica*, 229(4), 2018, 1551-1566.

[46] Onkar, A.K., Nonlinear buckling analysis of damaged laminated composite plates, *Journal of Composite Materials*, 53(22), 2019, 3111-3126.

[47] Ou, X., Zhang, X., Zhang, R., Yao, X., Han, Q., Weak form quadrature element analysis on nonlinear bifurcation and postbuckling of cylindrical composite laminates, *Composite Structures*, 188, 2018, 266-277.

[48] Zhou, Z., Ni, Y., Tong, Z., Zhu, S., Sun, J., Xu, X., Accurate nonlinear buckling analysis of functionally graded porous graphene platelet reinforced composite cylindrical shells, *International Journal of Mechanical Sciences*, 151, 2019, 537-550.

[49] Quan, T.Q., Cuong, N.H., Duc, N.D., Nonlinear buckling and post-buckling of eccentrically oblique stiffened sandwich functionally graded double curved shallow shells, *Aerospace Science and Technology*, 90, 2019, 169-180.

[50] Khoa, N.D., Thiem, H.T., Duc, N.D., Nonlinear buckling and postbuckling of imperfect piezoelectric S-FGM circular cylindrical shells with metal-ceramic-metal layers in thermal environment using Reddy's third-order shear deformation shell theory, *Mechanics of Advanced Materials and Structures*, 26(3), 2019, 248-259.

[51] Cho, H. K., Optimization of laminated composite cylindrical shells to maximize resistance to buckling and failure when subjected to axial and torsional loads, *International Journal of Precision Engineering and Manufacturing*, 19(1), 2018, 85-95.

[52] Tsiatas, G.C., Siokas, A.G., Sapountzakis, E.J., A Layered Boundary Element Nonlinear Analysis of Beams. *Frontiers in Built Environment: Computational Methods in Structural Engineering*, 4(52), 2018.

[53] Tsiatas, G.C., Babouskos, N.G., Linear and Geometrically Nonlinear Analysis of Non-Uniform Shallow Arches under a Central Concentrated Force, *International Journal of Non-Linear Mechanics*, 92, 2017, 92-101.

[54] Liang, C., Rogers, C. A., Design of Shape Memory Alloy Springs with Applications in Vibration Control, *Journal of Intelligent Material Systems and Structures*, 8(4), 1997, 314-322.

[55] McCormick, J., Tyber, J., DesRoches, R., Gall, K., Maier, H.J., Structural Engineering with Niti. Part II: Mechanical Behaviour and Scaling, *Journal of Engineering Mechanics*, 133(9), 2007, 1019-1029.

[56] Katsikadelis, J.T., *The Boundary Element Method for Engineers and Scientists*, Academic Press, Elsevier, Oxford, UK, 2016.

[57] Sanders, J.L., Nonlinear Theories of Thin Shells. *Quarterly Applied Mathematics*, 21, 1963, 21-36.

[58] Timoshenko, S., Woinowsky-Krieger, S., *Theory of plates and shells*, McGraw-Hill, 1959.

[59] Reddy, J.N., *Mechanics of Laminated Composite Plates and Shells. Theory and Analysis*, CRC Press, Florida, USA, 2003.

[60] Reddy, J.N., Mahaffey, P., Generalized beam theories accounting for von Kármán nonlinear strains with application to buckling, *Journal of Coupled Systems and Multiscale Dynamics*, 1(1), 2013, 120-134.

[61] Sapountzakis, E.J., Mokos, V.G., Shear deformation effect in nonlinear analysis of spatial beams, *Engineering Structures*, 30, 2008, 653-663.

[62] Liu, N., Jeffers, A.E., Isogeometric analysis of laminated composite and functionally graded sandwich plates based on a layerwise displacement theory, *Composite Structures*, 176, 2017, 143-153.

[63] Liu, N., Jeffers, A.E., Adaptive isogeometric analysis in structural frames using a layer-based discretization to model spread of plasticity, *Computers & Structures*, 196, 2018, 1-11.

[64] Liu, N., Jeffers, A.E., A geometrically exact isogeometric Kirchhoff plate: Feature-preserving automatic meshing and C^1 rational triangular Bézier spline discretizations, *International Journal for Numerical Methods in Engineering*, 115, 2018, 395-409.

[65] Powell, M.J.D., A Fortran subroutine for solving systems of Nonlinear algebraic equations, *Numerical Methods for Nonlinear Algebraic Equations*, P. Rabinowitz, ed., Gordon and Breach, 115-161, 1970.


[66] Batoz, J.L., Dhatt, G., Incremental displacement algorithms for nonlinear problems. *International Journal for Numerical Methods in Engineering*, 14(8), 1979, 1262-1267.


[67] Liu, N., Plucinsky, P., Jeffers, A.E., Combining Load-Controlled and Displacement-Controlled Algorithms to Model Thermal-Mechanical Snap-Through Instabilities in Structures, *Journal of Engineering Mechanics*, 143, 2017, 04017051.


[68] Liu, N., Jeffers, A.E., Feature-preserving rational Bézier triangles for isogeometric analysis of higher-order gradient damage models, *Computer Methods in Applied Mechanics and Engineering*, 357, 2019, 112585.

- [69] Tsiatas, G.C., Charalampakis, A.E., Optimizing the natural frequencies of axially functionally graded beams and arches, *Composite Structures*, 160, 2017, 256-266.
- [70] Charalampakis, A.E., Tsiatas, G.C., A Simple Rate-Independent Uniaxial Shape Memory Alloy (SMA) Model, *Frontiers in Built Environment: Computational Methods in Structural Engineering*, 4(46), 2018.
- [71] Zhang, Y., Zhu, S., A shape memory alloy-based reusable hysteretic damper for seismic hazard mitigation, *Smart Materials and Structures*, 16, 2007, 1603-1613.
- [72] Pi, Y.-L., Bradford, M.A., Uy, B., In-plane stability of arches, *International Journal of Solids and Structures*, 39(1), 2002, 105-125.

ORCID iD

George C. Tsiatas  <https://orcid.org/0000-0003-4808-7881>

Ioannis N. Tsiptsis  <https://orcid.org/0000-0001-6666-8474>

Antonis G. Siokas  <https://orcid.org/0000-0003-4735-4327>



© 2020 by the authors. Licensee SCU, Ahvaz, Iran. This article is an open access article distributed under the terms and conditions of the Creative Commons Attribution-NonCommercial 4.0 International (CC BY-NC 4.0 license) (<http://creativecommons.org/licenses/by-nc/4.0/>).